

# Optical Engineering

OpticalEngineering.SPIEDigitalLibrary.org

## **Comparative study on submillimeter flaws in stitched T-joint carbon fiber reinforced polymer by infrared thermography, microcomputed tomography, ultrasonic c-scan and microscopic inspection**

Hai Zhang  
Ulf Hassler  
Marc Genest  
Henrique Fernandes  
Francois Robitaille  
Clemente Ibarra-Castanedo  
Simon Joncas  
Xavier Maldague

# Comparative study on submillimeter flaws in stitched T-joint carbon fiber reinforced polymer by infrared thermography, microcomputed tomography, ultrasonic c-scan and microscopic inspection

Hai Zhang,<sup>a,\*</sup> Ulf Hassler,<sup>b</sup> Marc Genest,<sup>c</sup> Henrique Fernandes,<sup>a</sup> Francois Robitaille,<sup>d</sup> Clemente Ibarra-Castanedo,<sup>a</sup> Simon Joncas,<sup>e</sup> and Xavier Maldague<sup>a</sup>

<sup>a</sup>Laval University, Department of Electrical and Computer Engineering, Computer Vision and Systems Laboratory, 1065 Avenue de la Medecine, Quebec G1V 0A6, Canada

<sup>b</sup>Fraunhofer IIS, Fraunhofer Development Center X-ray Technologies (EZRT), Department of Application Specific Methods and Systems (AMS), Flugplatzstrasse 75, Fuerth 90768, Germany

<sup>c</sup>National Research Council Canada, Aerospace Portfolio, Structures, Materials and Manufacturing, 1200 Montreal Road, Ottawa K1A 0R6, Canada

<sup>d</sup>University of Ottawa, Department of Mechanical Engineering, 161 Louis Pasteur, Ottawa K1N 6N5, Canada

<sup>e</sup>Ecole de Technologie Superieure, Department of Automated Manufacturing Engineering, 1100 rue Notre-Dame Ouest, Montreal H3C 1K3, Canada

**Abstract.** Stitching is used to reduce dry-core (incomplete infusion of T-joint core) and reinforce T-joint structure. However, it may cause new types of flaws, especially submillimeter flaws. Microscopic inspection, ultrasonic c-scan, pulsed thermography, vibrothermography, and laser spot thermography are used to investigate the internal flaws in a stitched T-joint carbon fiber-reinforced polymer (CFRP) matrix composites. Then, a new microlaser line thermography is proposed. Microcomputed tomography (microCT) is used to validate the infrared results. A comparison between microlaser line thermography and microCT is performed. It was concluded that microlaser line thermography can detect the internal submillimeter defects. However, the depth and size of the defects can affect the detection results. The microporosities with a diameter of less than 54  $\mu\text{m}$  are not detected in the microlaser line thermography results. Microlaser line thermography can detect the microporosity (a diameter of 0.162 mm) from a depth of 90  $\mu\text{m}$ . However, it cannot detect the internal microporosity (a diameter of 0.216 mm) from a depth of 0.18 mm. The potential causes are given. Finally, a comparative study is conducted.

© 2015 Society of Photo-Optical Instrumentation Engineers (SPIE) [DOI: [10.1117/1.OE.54.10.104109](https://doi.org/10.1117/1.OE.54.10.104109)]

Keywords: laser line thermography; x-ray computed tomography; ultrasonic c-scan; nondestructive testing; T-joint.

Paper 150792P received Jun. 11, 2015; accepted for publication Sep. 21, 2015; published online Oct. 15, 2015.

## 1 Introduction

Three-dimensional (3-D) carbon fiber-reinforced polymer (CFRP) matrix composites are increasingly used for aircraft construction due to their exceptional stiffness and strength-to-mass ratios. Composites made from 3-D textile preforms can reduce both the weight and manufacturing cost of advanced composite structures within aircraft, naval vessels, and the blades of wind turbines.<sup>1</sup> The in-plane stiffness and strength of 3-D woven composites were found to be lower, while the out-of-plane properties were higher compared with conventional two-dimensional laminates.<sup>2</sup> The assembly of 3-D complex composite structures indicates the need for efficient joining methods. The most frequently used joint found in structural applications is the T-joint.

The purpose of T-joints is to transfer flexural, tension, and shear loads to the skin. T-stiffeners are extensively used in aircraft wings in order to prevent skin buckling during wing loading. However, designing composite joints is more difficult than metallic joints due to the mechanical properties of composite materials.<sup>3</sup>

In the design of T-joints, filler is inserted in T-joints and resin is used to reinforce the structure. The fiber insertion

technique has the potential of creating a low-cost T-joint with improved damage tolerance and failure strength.<sup>4</sup> However, incomplete infusion of T-joints core (dry-core) is an essential issue. Figure 1 shows a typical dry-core in a nonstitched 3-D T-joint CFRP.

Stitching<sup>5</sup> is used to reduce dry-core and reinforce T-joint structure.<sup>6</sup> However, stitching might cause new types of flaws due to the characteristic of the structure. The corresponding study was poorly documented, especially using nondestructive testing (NDT). NDT of composite materials is complicated due to the wide range of flaws encountered (including delamination, microcracking, fiber fracture, fiber pullout, matrix cracking, inclusions, voids, and impact damage). The ability to quantitatively characterize the type, geometry, and orientation of flaws is essential.<sup>7</sup> The ability to identify and characterize such submillimeter flaws accurately is a challenge.

In this paper, microscopic inspection, ultrasonic c-scan, pulsed thermography, vibrothermography, and laser spot thermography using the lock-in method are performed to detect a stitched 3-D T-joint CFRP. A new microlaser line thermography is proposed; 18- $\mu\text{m}$  resolution x-ray computed

\*Address all correspondence to: Hai Zhang, E-mail: [hai.zhang.1@ulaval.ca](mailto:hai.zhang.1@ulaval.ca)

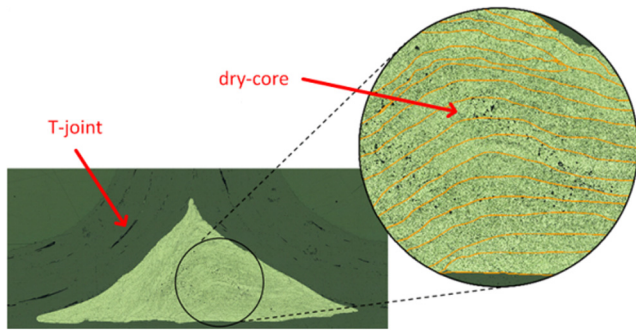


**Fig. 1** A typical dry-core in a nonstitched three-dimensional (3-D) carbon fiber-reinforced polymer (CFRP) (microscopic inspection).

tomography (CT) is used to validate the detection results. A comparison between microlaser line thermography and high-resolution x-ray CT is performed. It was found that microlaser line thermography can detect the submillimeter internal defects in the sample. However, the depth and size of defects can affect the detection results. The microporosities with a diameter of less than  $54\text{ }\mu\text{m}$  were not detected in the microlaser line thermography results. Microlaser line thermography can detect the microporosity (a diameter of  $0.162\text{ mm}$ ) from a depth of  $90\text{ }\mu\text{m}$ , but cannot detect the microporosity (a diameter of  $0.216\text{ mm}$ ) from a depth of  $0.18\text{ mm}$ . The potential causes are discussed. Finally, a comparative study is conducted.

## 2 Specimen

The complete stitched 3-D T-joint CFRP is shown in Fig. 2(a). The sample contains six stitching lines. The purpose of the stitching is to consolidate the T-joint structure and to reduce dry-core. The sample measures  $152\text{ mm}$  in length,  $148\text{ mm}$  in width,  $63\text{ mm}$  in height, and  $5\text{ mm}$  in thickness (excluding the T-stringer).

The front side of the sample is shown in Fig. 2(b). The sample was detected using ultrasonic c-scan, pulsed thermography, and vibrothermography before microscopic inspection. Then, a  $30\text{ mm} \times 148\text{ mm}$  part was cut and polished for microscopic inspection. Finally, a  $10\text{ mm} \times 152\text{ mm}$  zone was detected using microlaser line thermography and high-resolution x-ray tomography.

## 3 Methods and Results

### 3.1 Microscopic Inspection

Microscopic inspection was performed through cutting and polishing a part measuring  $30\text{ mm} \times 148\text{ mm}$ , shown in Fig. 2(b). The purpose is to investigate the structure and internal flaws in the sample. The grinding and polishing procedure is automated, as is the procedure for the stitching of many images obtained by autofocal and self-traveling microscope. These procedures are thus automated, but they require supervision. Images are obtained using optical as opposed to scanning electron microscope, which requires polishing instead of gold sputtering. However, the overall time required for either device is probably comparable and the optical method is far more accessible. The physical size corresponding to the assembled image is about  $12\text{ mm} \times 12\text{ mm}$ , which is the largest that can be accommodated. The resolution of the inspection is  $7\text{ }\mu\text{m}$ . The quality of the images is good and sufficient for inspection. There are scratches, watermarks, and dirt on these first images but these can be sorted.

The microscopic inspection results are shown in Fig. 3. Figure 3(a) shows the microporosities in the top section. Figure 3(b) shows the stitching and microporosities in cross section. In Fig. 3(b), more microporosities in the resin redundancy zone are inspected than in other zones. Most microporosities measure a diameter of about  $0.1\text{ mm}$  to  $0.2\text{ mm}$ , as shown in Fig. 3.

### 3.2 Ultrasonic C-scan

Ultrasonic c-scan is a well-established NDT method that has the ability to detect flaws in either the partial or entire thickness of the materials.<sup>8</sup> It has been widely used to detect flaws in metals.<sup>9</sup> It is also increasingly used to detect composites due to its flexibility and convenience.

It is a challenge to detect thick 3-D CFRP using ultrasonic c-scan due to the CFRP complex internal structure. The complex internal structure can cause attenuation and scattering of ultrasonic beams.<sup>10</sup> Ultrasonic c-scan has been widely used to detect voids and laminates in composites.<sup>11</sup> However, submillimeter flaw detection was poorly documented.

Ultrasonic c-scan was performed to detect the entire sample. The water immersion method was used. The detection results using the transducer with the frequency of

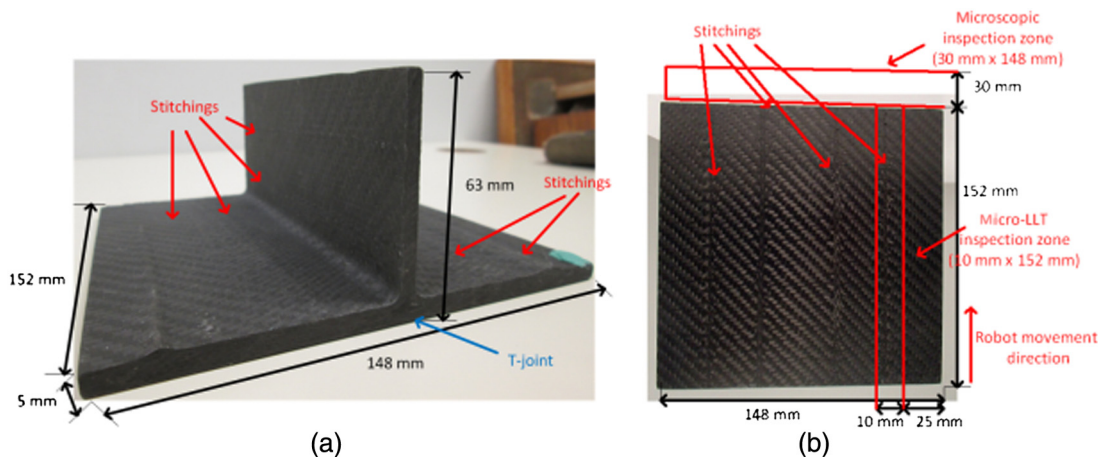


**Fig. 2** (a) Complete stitched 3-D T-joint sample, (b) front side of the sample.



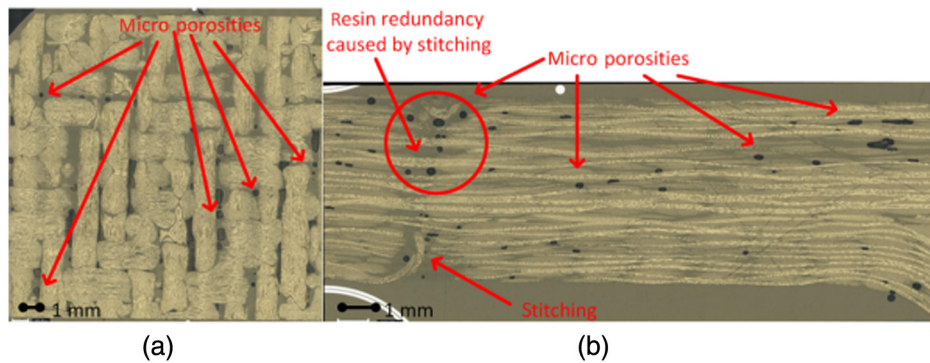


**Fig. 3** Microscopic inspection results: (a) top section and (b) cross section.

2.25 MHz are shown in Fig. 4. The images were acquired before the microscopic inspection. Figure 4(a) shows the detection result using the pulsed-echo technique, which uses a transducer to emit ultrasonic beams, and uses the same transducer to receive the reflected signals. Figure 4(b) shows the detection result using the through-transmission technique, which uses a transducer to emit ultrasonic beams, and uses another transducer with the same parameters to receive the transmitted signals on the opposite side. Figure 4(c) shows the color scale for the signal amplitude percentage.

In Fig. 4(a), many abnormalities are detected. Some of them might be voids and porosities. However, it is a challenge to identify and characterize them due to the attenuation and scattering of the ultrasonic beams, which are caused by the complex internal structure. In Fig. 4(b), three large-sized abnormalities are shown. They might be resin abnormalities

or internal structural flaws. However, they are also difficult to identify and accurately characterize. Ultrasonic c-scan using transducers with frequencies of 5, 10, and 15 MHz was also performed. However, none of the scans can identify and accurately characterize the internal flaws.

### 3.3 Pulsed Thermography

Infrared thermography is increasingly used to detect composites. In the past few years, a great number of new infrared thermography methods have been proposed, such as eddy-current thermography, induction thermography, vibro-thermography, and so on.<sup>12,13</sup> However, submillimeter flaw detection using infrared thermography was still poorly documented.

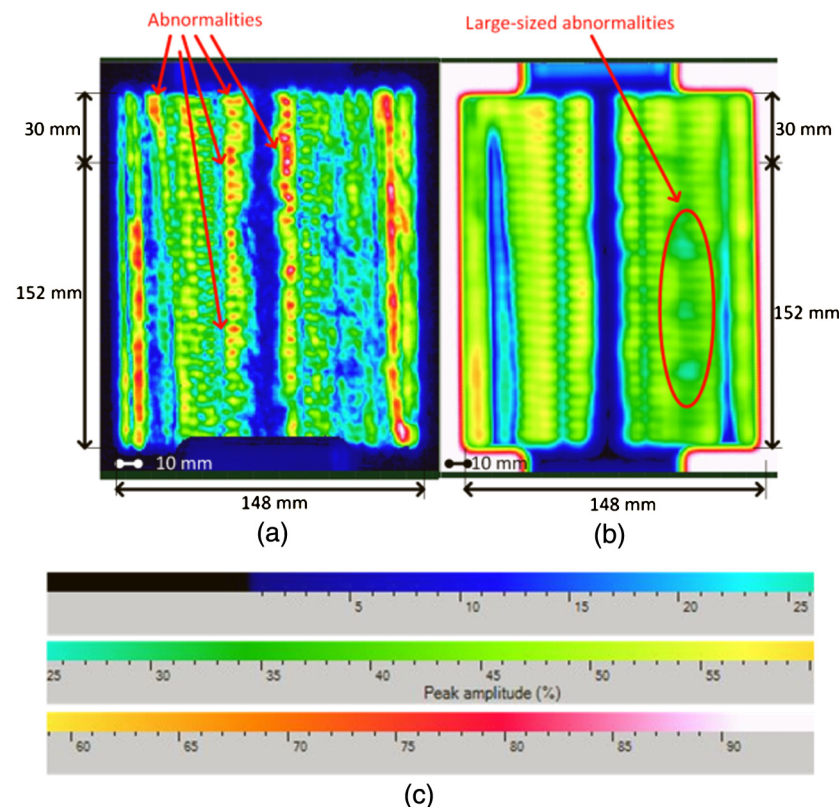


**Fig. 4** Ultrasonic c-scan results (2.25 MHz): (a) pulsed-echo, (b) through-transmission, and (c) color scale for signal amplitude percentage.

Pulsed thermography is a classical NDT method. Pulsed thermography was used to detect flaws in monomaterials in its early period. In the past two decades, many studies have focused on the detection on flaws in composites. In 1996, Maldague and Marinetti proposed pulsed phase thermography to process pulsed thermography data.<sup>14</sup> Pulsed thermography is currently becoming a classical NDT method in the aerospace industry.

In pulsed thermography, usually a high-energy flash lamp is used to generate a uniform plane heating source on the sample surface. The heat travels through the inspected material to the subsurface anomalies (defects or damages) and back to the surface. When the pulse heat flux is applied to the sample surface, an out-of-plane heat flow is generated in the sample. The uniform temperature increase is observed on the surface, if the sample has no defects. If the sample has defects such as voids and delamination damage, a localized high-temperature region appears on the sample surface just above the defect due to the insulation effect of the defects. The shape of the high-temperature region reflects the defect shape under the surface. The location, shape, and size of the defect can be estimated from the temperature distribution on the sample surface.<sup>12,13</sup>

Pulsed thermography was performed to detect the sample. Figure 5(a) shows the classical pulsed thermography setup.<sup>13</sup> Figure 5(b) shows the experimental setup. In the setup, a midwave infrared (MWIR) camera (FLIR Phoenix, InSb,  $3 - 5 \mu\text{m}$ ,  $640 \times 512$  pixels) at a frame rate of 55 Hz was used to record the temperature profile. Two photographic flashes (Balcar FX 60 with pulse duration of 5 ms and producing 6.4 kJ per flash) were used to heat the sample.

Figure 6 shows the detection results before the microscopic inspection. Figure 6(a) shows the image from first derivative image processing. Figure 6(b) shows the image from second derivative image processing. In Fig. 6, some voids measured around 1 to 2 mm are inspected. Pulsed thermography can detect large-sized flaws. However, it is a challenge to characterize submillimeter flaws. Several image

processing methods were conducted. However, none of them can identify and characterize submillimeter flaws.

### 3.4 Vibrothermography

Vibrothermography, also known as ultrasonic thermography or thermosonics, utilizes mechanical waves to directly stimulate internal defects without heating the surface as in optical methods such as lock-in thermography and pulsed thermography. In classical ultrasound testing, a transducer is placed in contact with the sample with the help of coupling media. The ultrasonic waves travel through the specimen and are transmitted back to the surface where the transducer picks up the reflected signal (pulsed-echo technique), or they are collected on the opposite side (transmission). The principle of defect detection is based on the differences in specific acoustic impedances between materials. In vibrothermography, ultrasonic waves travel freely through a homogeneous material, whereas an internal defect produces a complex combination of absorption, scattering, beam spreading, and dispersion of the waves, whose primary manifestation will be in the form of heat. Heat then travels by conduction in all directions; an infrared camera can be directed to one of the surfaces of the specimen to capture the defect signature.<sup>13</sup>

Figure 7(a) shows the classical vibrothermography setup.<sup>13</sup> Figure 7(b) shows the experimental setup. In the setup, an MWIR camera (FLIR Phoenix, InSb,  $3 - 5 \mu\text{m}$ ,  $640 \times 512$  pixels) at a frame rate of 55 Hz was used to record the temperature profile. The transducer horn was pressed against the sample and a burst of ultrasound wave (20 kHz, 2200 W) at a modulation frequency of 0.25 Hz and with amplitude modulated between 10% and 30% of maximum power was delivered to the sample.

Figure 8 shows the detection results before the microscopic inspection. None of the two images can identify flaws. The potential reason is heat source coupling caused by the complex internal structure.

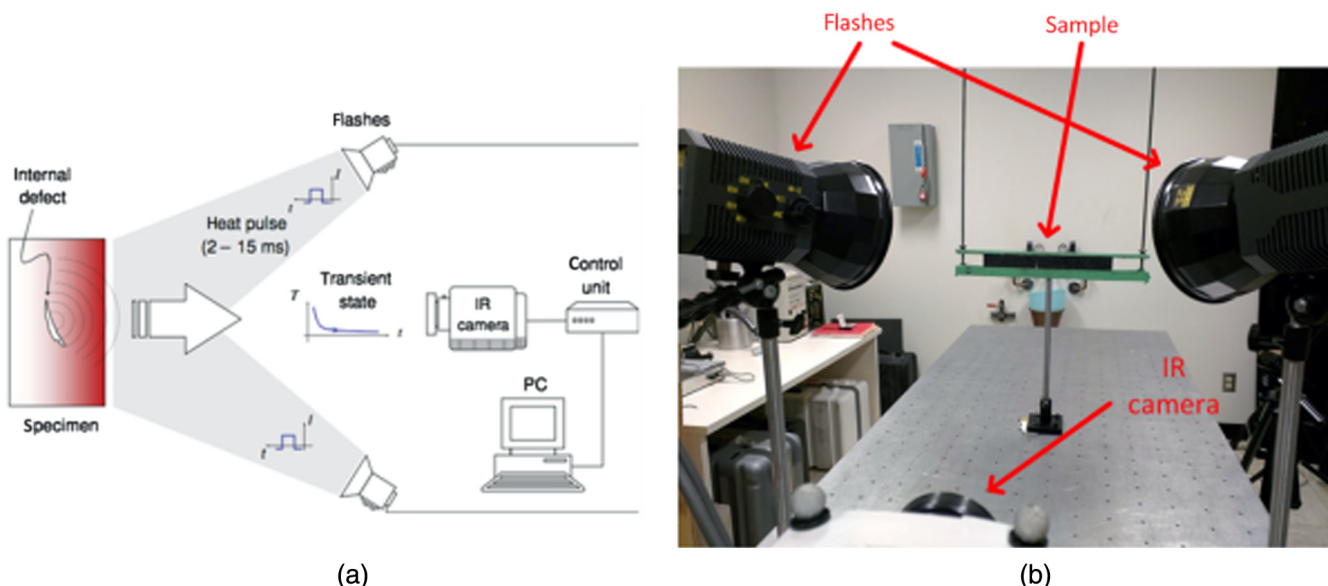


Fig. 5 (a) Classical pulsed thermography setup<sup>13</sup> and (b) experimental setup.

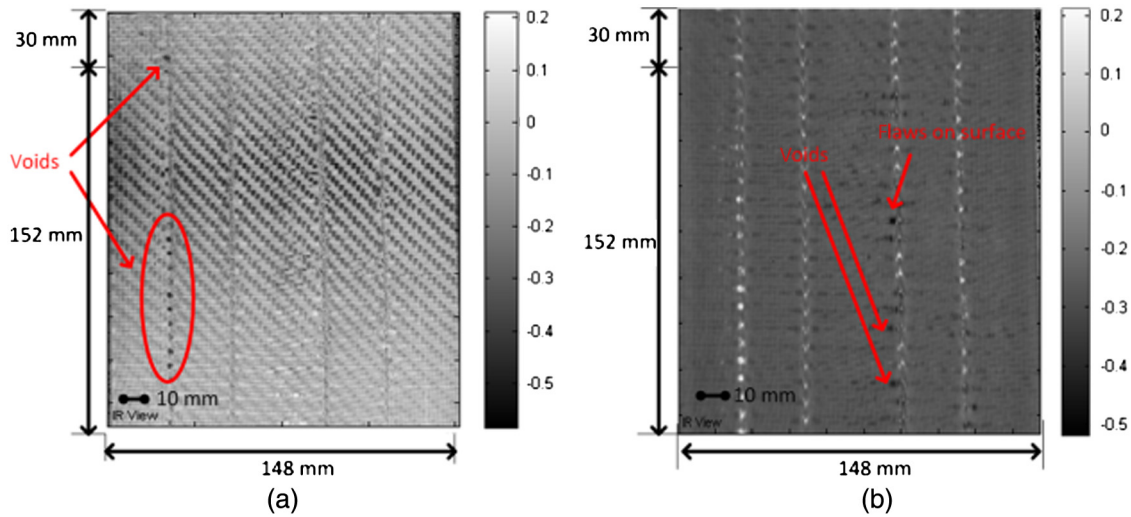


Fig. 6 Pulsed thermography results: (a) first derivative and (b) second derivative.

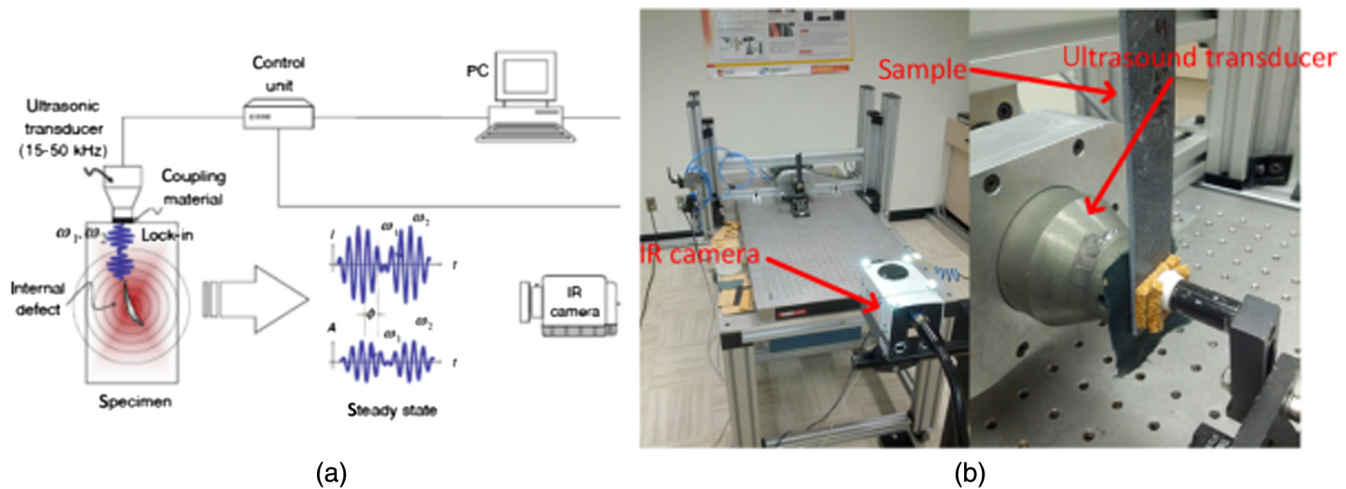


Fig. 7 (a) Classical vibrothermography setup<sup>13</sup> and (b) experimental setup.

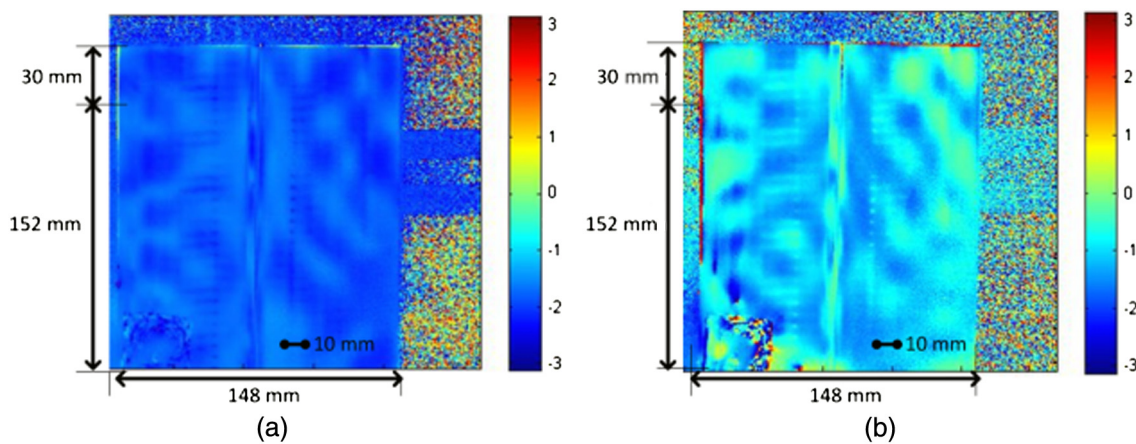


Fig. 8 Vibrothermography results.



### 3.5 Laser Spot Thermography and Lock-in Thermography

Laser spot thermography has been used to detect surface cracks and fiber orientation in composites. Surface crack detection using laser spot thermography was reported in 2007.<sup>15,16</sup> Fiber orientation detection using laser spot thermography was reported in 2013.<sup>17,18</sup> Further studies on surface cracks<sup>19–21</sup> and fiber orientation<sup>22,23</sup> were recently reported.

Figure 9(a) shows the classical laser spot thermography setup.<sup>13</sup> Figure 9(b) shows the experimental setup. In the setup, an MWIR camera (FLIR Phoenix, InSb,  $3 - 5 \mu\text{m}$ ,  $640 \times 512$  pixels) at a frame rate of 55 Hz was used to record the temperature profile. A diode-laser was used for heating source. The laser wavelength is 805 nm. The laser beam power is 4.2 W. A convex lens was used to focalize the laser beam. A microlens was used to detect the submillimeter flaws. The magnification of the microlens is  $1\times$ . The lock-in method was used to identify and characterize the internal flaws.

Lock-in thermography, also known as modulated thermography, is a technique derived from photo thermal radiometry. In the latter, a small surface spot is periodically illuminated by an intensity-modulated laser beam to inject thermal waves into the specimen. The thermal response is recorded at the same time using an infrared detector and decomposed by a lock-in amplifier to extract the amplitude and phase of the modulation. Photo thermal radiometry is a raster point-by-point technique that requires long acquisition times, especially in the case of deep defects involving very low modulation frequencies. Furthermore, extra hardware such as a lock-in amplifier is needed in order to retrieve the amplitude and phase of the response. Heat diffusion through a solid is a complex 3-D problem that can be described by Fourier's law of heat diffusion:

$$\nabla^2 T - \frac{1}{\alpha} \cdot \frac{\partial T}{\partial t} = 0, \quad (1)$$

where  $T$  is the temperature,  $t$  is the time,  $\alpha = k/\rho c_p$  is the thermal diffusivity of the material being inspected,  $k$  is the thermal conductivity,  $\rho$  is the density, and  $c_p$  is the specific heat at constant pressure.

A four-point methodology for sinusoidal stimulation can be employed<sup>24,25</sup> to calculate the phase and amplitude from the response signal. Input and output have the same shape when sinusoids are used. There is only a change in amplitude and phase that can be calculated as follows:<sup>24</sup>

$$A = \sqrt{(S_1 - S_3)^2 + (S_2 - S_4)^2}, \quad (2)$$

$$\varphi = \arctan\left(\frac{S_1 - S_3}{S_2 - S_4}\right), \quad (3)$$

where  $A$  is the amplitude and  $\varphi$  is the phase. The four-point method is fast but it is valid only for sinusoidal stimulation and is affected by noise. The signal can be denoised in part by averaging several points instead of a single one and/or by increasing the number of cycles. Another possibility is to fit the experimental data using least-squares regression and to use this synthetic data to calculate the amplitude and the phase. These two alternatives contribute to slow down the calculations. Empirical expressions have been proposed to relate the depth of a given defect to the heat source frequency. The thermal diffusion length ( $\mu$ )<sup>26</sup> can be used to fit experimental data and estimate the depth ( $Z$ ) as proposed by<sup>27</sup>

$$Z = C_1 \sqrt{\frac{\alpha}{\pi f_b}} = C_1 \mu, \quad (4)$$

where  $Z$  is the depth of detection,  $\mu$  is the thermal diffusion length,  $\alpha$  is the diffusivity of the material or sound area  $S_a$ , and  $\alpha$  in CFRP is  $4.2 \times 10^{-7} \text{ (m}^2/\text{s)}$ , measured by Ibarra-Castaneda in 2005.<sup>27</sup>  $f_b$  is the blind frequency, while  $f_b$  is related to the time when defects become visible, and this is how the thermal images are generated for a given detection depth.  $C_1$  is a correlation constant. The reported values of  $C_1$  range from 1.5 to 2  $C_1 = 1.8$  are frequently adopted.<sup>13</sup>

Figure 10(a) shows the image prior to heating. The infrared image measures  $12 \text{ mm} \times 14 \text{ mm}$ . Point four is the heating spot shown in Fig. 10(b).

Figure 11(a) shows the detection result on the surface. Figure 11(b) shows the result from the depth of 0.21 mm,

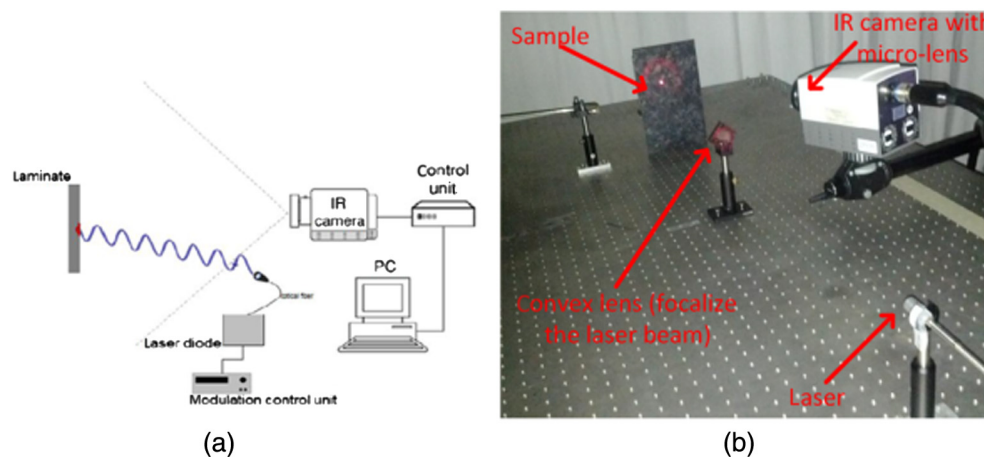


Fig. 9 (a) Classical laser spot thermography setup<sup>22</sup> and (b) experimental setup.<sup>17</sup>

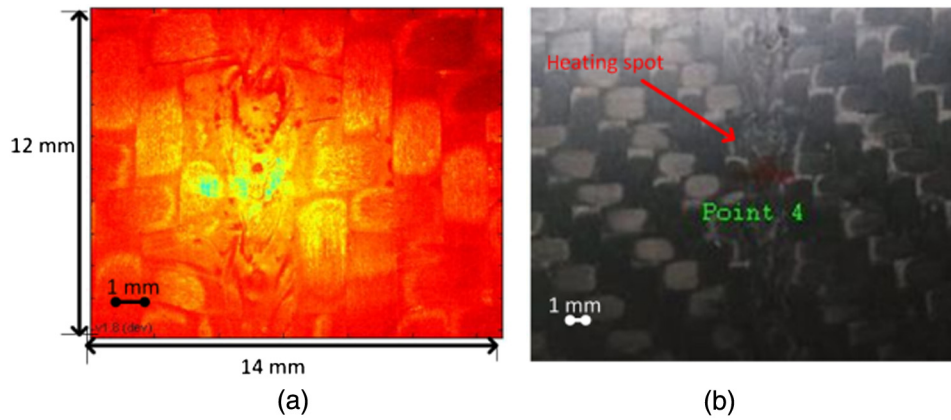


Fig. 10 (a) Image prior to heating and (b) heating spot.

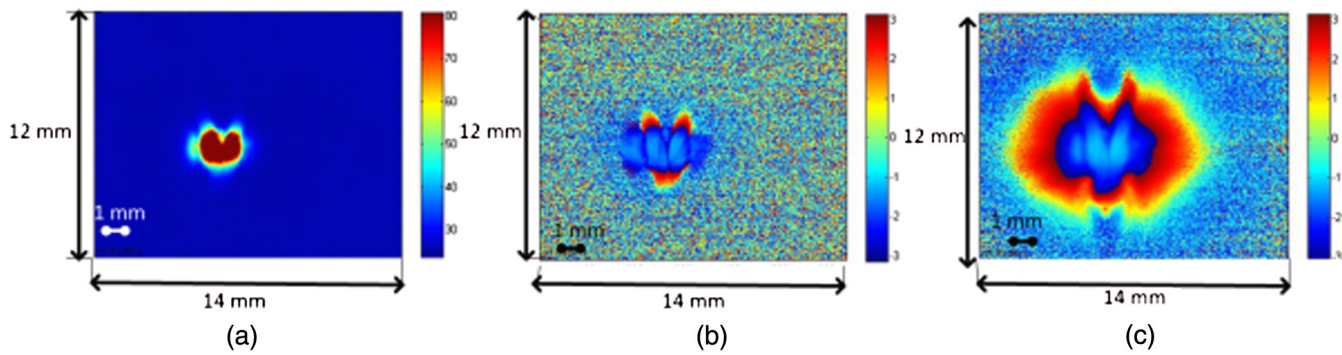


Fig. 11 Laser spot thermography results (locked-in method): (a) surface, (b) depth: 0.21 mm, and (c) depth: 0.65 mm.

and Figure 11(c) shows the result from the depth of 0.65 mm. The detected depths were calculated using Eq. (4). In Fig. 11, no defect is detected. Laser spot thermography can detect internal structure and flaws using the lock-in method. However, it is a time-consuming technique. It is difficult to detect the entire sample (152 mm  $\times$  148 mm) using laser spot thermography.

### 3.6 Microlaser Line Thermography and X-Ray Tomography

Laser line thermography has been used to detect surface cracks.<sup>28</sup> However, the detection of other types of flaws was poorly documented. Li et al. used a beam expander and a cylindrical lens to convert a laser spot with a radius of around 0.9 mm to a laser line source.<sup>28</sup> In this paper, the authors used a galvanometer scanning mirror with a frequency of 600 Hz to generate a laser line.<sup>29</sup> A microlens was used to identify and characterize submillimeter flaws.

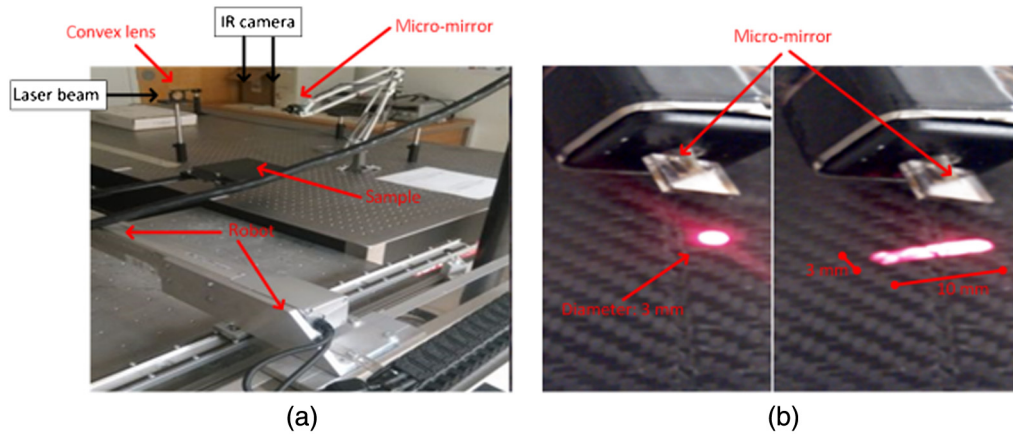
Figure 12(a) shows the experimental setup for microlaser line thermography. In the setup, the sample was fixed on a robot. An MWIR camera (FLIR Phoenix, InSb, 3 – 5  $\mu$ m, 640  $\times$  512 pixels) at a frame rate of 55 Hz was used to record the temperature profile. A diode-laser was used. The laser wavelength is 805 nm, the laser beam power is 2.9 W, and the heating time is 0.5 s. A convex lens was used to focalize the laser beam. A microlens was used to identify and characterize the submillimeter flaws; the magnification

of the microlens is 1 $\times$ . A galvanometer scanning mirror was mounted between the infrared (IR) camera and the sample. In Fig. 12(b), the laser spot was converted into a laser line when the galvanometer scanning mirror swung with the frequency of 600 Hz. Figure 12(b) shows the heating source of length around 10 mm and width is around 3 mm.

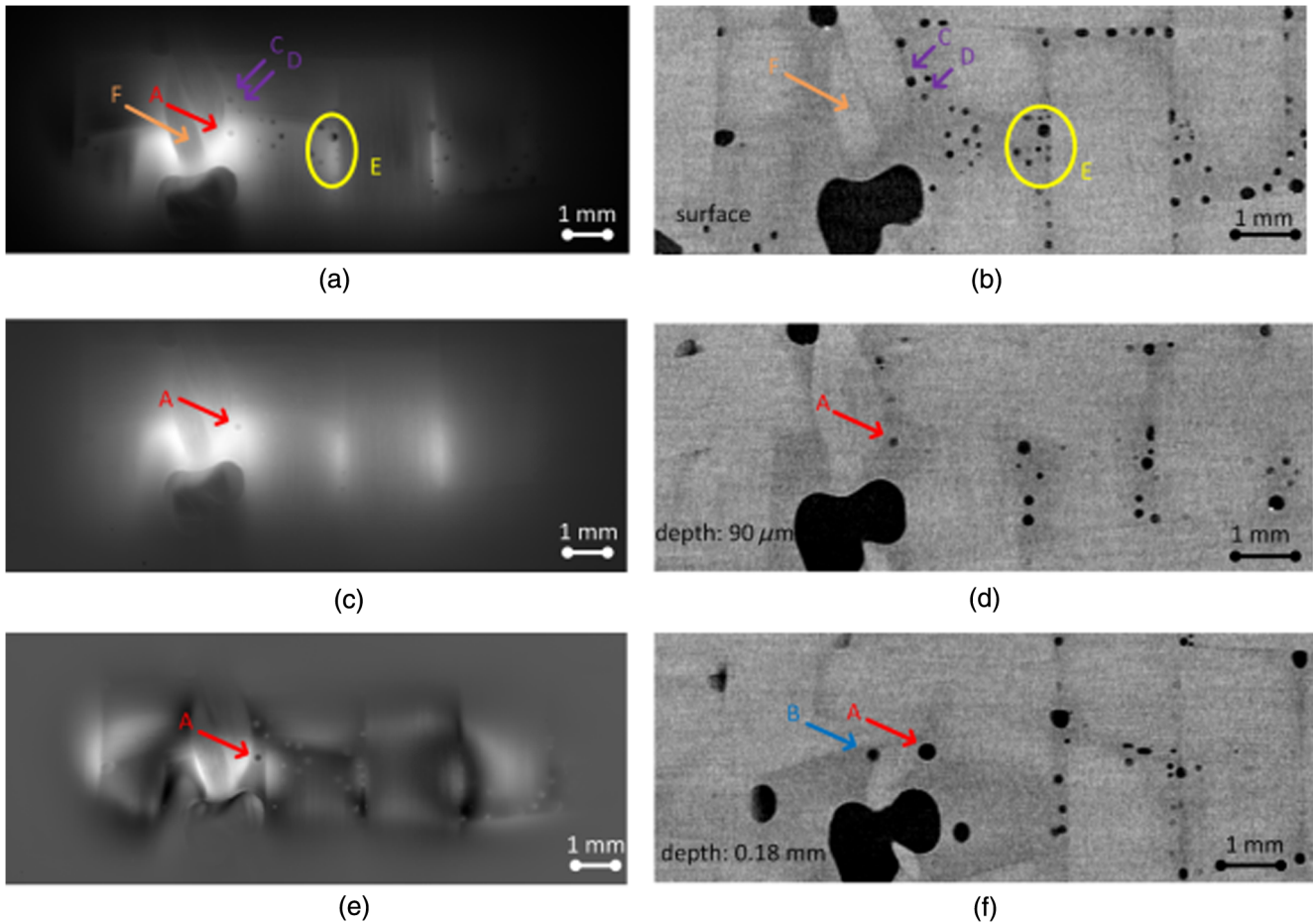
Figure 2(b) shows the detected zone. The laser line crosses a stitching line. The robot moved per 3 mm toward the direction shown in Fig. 2(b). A total of 51 tests were performed to detect the 10 mm  $\times$  152 mm area shown in Fig. 2(b). The method is defined as microlaser line thermography.

Figure 13 shows the comparison of microlaser line thermography results and high-resolution x-ray tomography results. Some specific microporosities are marked in the images. Figure 13(b) shows the surface image of a detected zone. The image was acquired using 18- $\mu$ m resolution x-ray tomography. Some microporosities are detected on the surface. Figure 13(a) shows the microlaser line thermography image in the same zone. The infrared image was from cold image subtraction. This image processing method is used to reduce the effects of fixed artifacts in a thermographic sequence, for example, reflections from the environment such as residual heating coming from the lamps and even the reflection from the camera that appears during the acquisition. Since these artifacts are more or less constant during the whole acquisition, including before heating when the image is “cold,” this image or the average of several





**Fig. 12** (a) Microlaser line thermography experimental setup and (b) laser spot to laser line.



**Fig. 13** (a) Microlaser line thermography result (cold image), (b) x-ray tomography result (surface), (c) microlaser line thermography result (contrast rectification), (d) x-ray tomography result (depth: 90  $\mu\text{m}$ ), (e) microlaser line thermography result (PCT), and (f) x-ray tomography result (depth: 0.18 mm).

images can be subtracted before heating, so their effect is reduced. In Fig. 13(a), some microporosities on the surface such as C and D (marked in purple) are detected. However, some other microporosities on the surface such as some in the zone E (marked in yellow) are not detected. The potential

cause is the infrared camera resolution limitation. The microporosities with a diameter of less than 54  $\mu\text{m}$  cannot be detected in Fig. 13(a).

In Fig. 13(a), the microporosity A (marked in red) is detected. However, it is not detected on the surface shown

in Fig. 13(b). It appears from the depth of 90  $\mu\text{m}$  shown in Fig. 13(d). Figure 13(d) shows the x-ray tomography image from the depth of 90  $\mu\text{m}$ . The microporosity A measures 0.162 mm in diameter. The microporosity A can be detected more clearly in the infrared image with the contrast rectification shown in Fig. 13(c). Figure 13(e) shows the infrared image from principal component thermography.<sup>30</sup> In Fig. 13(e), the performance of the microporosity A is exceptional (darker in contrast) compared to the other microporosities. These results confirm that microlaser line thermography can detect the internal submillimeter defects in the sample. However, the depth and the size of defects can affect the detection results.

Figure 13(f) shows the x-ray tomography image from 0.18 mm depth. The microporosity A measures 0.306 mm in diameter from 0.18 mm depth. The microporosity B (marked in blue) is detected. It measures 0.216 mm in diameter from a depth of 0.18 mm. However, the microporosity B cannot be detected in the infrared images. One potential cause is that the depth of 0.18 mm exceeds the IR camera detection limitation with the laser power of 2.9 W. Another potential cause is that the microporosity B is below the fiber F (marked in orange) shown in Figs. 13(a) and 13(b). This might reduce the heat diffusion. A finite-element simulation could be contributive to the analysis.

#### 4 Conclusion

In this paper, several techniques were used to detect a stitched 3-D T-joint CFRP. Microscopic inspection can obtain the internal structure and submillimeter flaws in a clear manner. However, it is a time-consuming and destructive technique. Ultrasonic c-scans cannot identify and accurately characterize the internal flaws. Pulsed thermography can detect the large-sized flaws, but cannot detect the submillimeter flaws. Vibrothermography cannot detect the internal flaws due to the CFRP's complex structure. Laser spot thermography using the lock-in method can detect the internal structure and flaws. However, it is a time-consuming technique.

A new microlaser line thermography was defined; 18- $\mu\text{m}$  resolution x-ray tomography was used to validate the microlaser line thermography results. A comparison of microlaser line thermography and high-resolution x-ray tomography was conducted. It was concluded that microlaser line thermography can detect the internal submillimeter defects in the sample. However, the depth and size of the defects can affect the detection results. The microporosities with a diameter of less than 54  $\mu\text{m}$  cannot be detected in the microlaser line thermography results. Microlaser line thermography can detect the microporosity (a diameter of 0.162 mm) from a depth of 90  $\mu\text{m}$ . However, it cannot detect the internal microporosity (a diameter of 0.216 mm) from the depth of 0.18 mm. One potential cause is that the depth of 0.18 mm exceeds the IR camera detection limitation with the laser beam power of 2.9 W. Another potential cause is that the microporosity from the depth of 0.18 mm is below a fiber. It might reduce the heat diffusion. A finite-element simulation could be contributive to the analysis.

#### Acknowledgments

This research is supported by Consortium for Research and Innovation in Aerospace in Quebec (CRIAQ) through

Project Nos. CRIAQ COMP-501—CRDPJ 408010-10. The authors would like to acknowledge the financial support to the project provided by Bell Helicopter (Canada) Inc. and Bombardier Inc. The authors would like to acknowledge the support provided by the Canada Research Chair in Multipolar Infrared Vision (MiViM) and the industrial partners: Delastek Inc., Hutchinson Inc., Texonic Inc., CTT group. The authors would also like to thank Wolfgang Holub from Fraunhofer EZRT (Germany), Michael Brothers from National Research Council (Canada), Lucas West from the University of Ottawa (Canada), and Catherine Leduc from Ecole de Technologie Supérieure (Canada) for their assistance.

#### References

1. F. Stig, "3D-woven reinforcement in composites," PhD Thesis, KTH Royal Institute of Technology, Stockholm, Sweden (2012).
2. F. Stig and S. Hallström, "Assessment of the mechanical properties of a new 3D woven fibre composite material," *Compos. Sci. Technol.* **69**(11), 1686–1692 (2009).
3. J. Ekh, "Multi-fastener single-lap joints in composite structures," PhD Thesis, KTH Royal Institute of Technology, Stockholm, Sweden (2006).
4. P. Stöckler and M. Ramulu, "Investigation of mechanical behavior of transverse stitched T-joints with PR520 resin in flexure and tension," *Compos. Struct.* **52**(3), 307–314 (2001).
5. P. Potluri, E. Kusak, and T. Reddy, "Novel stitch-bonded sandwich composite structures," *Compos. Struct.* **59**(2), 251–259 (2003).
6. T. J. Kang and S. H. Lee, "Effect of stitching on the mechanical and impact properties of woven laminate composite," *J. Compos. Mater.* **28**(16), 1574–1587 (1994).
7. Y. Bar-Cohen, "Emerging NDT technologies and challenges at the beginning of the third millennium, part 2," *Mater. Eval.* **58**(2), 141–150 (2000).
8. C. Hellier, *Handbook of Nondestructive Evaluation*, McGraw-Hill, Boston, Massachusetts (2001).
9. A. Pippard, "Theory of ultrasonic attenuation in metals and magnetoacoustic oscillations," in *Proc. Royal Society of London A: Mathematical, Physical and Engineering Sciences*, Vol. 257(1289), pp. 165–193, The Royal Society (1960).
10. H. Jeong and D. Hsu, "Experimental analysis of porosity-induced ultrasonic attenuation and velocity change in carbon composites," *Ultrasonics* **33**(3), 195–203 (1995).
11. C. Tsao and H. Hocheng, "Computerized tomography and c-scan for measuring delamination in the drilling of composite materials using various drills," *Int. J. Mach. Tools Manuf.* **45**(11), 1282–1287 (2005).
12. X. Maldague, *Theory and Practice of Infrared Technology for Nondestructive Testing*, Wiley, New York (2001).
13. H. Czichos, *Handbook of Technical Diagnostics*, Springer, Verlag Berlin Heidelberg (2013).
14. X. Maldague and S. Marinetti, "Pulse phase infrared thermography," *J. Appl. Phys.* **79**(5), 2694–2698 (1996).
15. S. E. Burrows et al., "Combined laser spot imaging thermography and ultrasonic measurements for crack detection," *Nondestruct. Test. Eval.* **22**(2–3), 217–227 (2007).
16. A. Rashed et al., "Crack detection by laser spot imaging thermography," in *Review of Progress in Quantitative Nondestructive Evaluation*, 894(1), 500–506, American Institute of Physics Publishing, Portland, Oregon (2007).
17. H. Fernandes and X. Maldague, "Use of infrared thermography to measure fiber orientation on carbon-fiber reinforced composites," in *Proc. ISEM*, Quebec, Canada, pp. 275–280 (2013).
18. H. Fernandes and X. Maldague, "Fiber orientation assessment in carbon fiber reinforced composites using infrared thermography," in *Proc. ICCM*, Montreal, Canada, S. V. Hoa and P. Hubert, Eds., Vol. 1, pp. 4970–4977 (2013).
19. J. Schlichting et al., "Imaging cracks by laser excited thermography," in *Review of Progress in Quantitative Nondestructive Evaluation*, 1211(1), pp. 727–734, American Institute of Physics, Kingston, Rhode Island (2010).
20. J. Schlichting, C. Maierhofer, and M. Kreutzbruck, "Crack sizing by laser excited thermography," *NDT E Int.* **45**(1), 133–140 (2012).
21. B. Weekes et al., "The effect of crack opening on thermosonics and laser-spot thermography," in *Review of Progress in Quantitative Nondestructive Evaluation*, 1211(1), 490–497, American Institute of Physics Publishing, Kingston, Rhode Island (2010).
22. H. C. Fernandes and X. P. Maldague, "Fiber orientation assessment on surface and beneath surface of carbon fiber reinforced composites using active infrared thermography," *Proc. SPIE* **9105**, 91050D (2014).

23. H.-C. Fernandes and X. Maldague, "Fiber orientation assessment in complex shaped parts reinforced with carbon fiber using infrared thermography," *Quant. Infr. Therm. J.* **12**(1), 1–16 (2015).
24. L. D. Favro and X. Han, "Thermal wave materials characterization and thermal wave imaging," in *Sensing for Materials Characterization, Processing and Manufacturing, ASNT TONES*, Vol. **1**, pp. 399–415, The American Society for Nondestructive Testing, Inc., Columbus, Ohio (1998).
25. G. Busse, "Techniques of infrared thermography: Part 4 lockin thermography," in *Nondestructive Handbook, Infrared and Thermal Testing*, X. Maldague and P. O. Moore, Eds., 3rd ed., Vol. **3**, pp. 318–327, The American Society for Nondestructive Testing—ASNT Press, Columbus, Ohio (2001).
26. G. Busse and A. Rosencwaig, "Subsurface imaging with photoacoustics," *Appl. Phys. Lett.* **36**(10), 815 (1980).
27. C. I. Castanedo, "Quantitative subsurface defect evaluation by pulsed phase thermography: depth retrieval with the phase," PhD Thesis, Université Laval (2005).
28. T. Li, D. P. Almond, and D. A. S. Rees, "Crack imaging by scanning laser-line thermography and laser-spot thermography," *Meas. Sci. Technol.* **22**(3), 035701 (2011).
29. H. Zhang et al., "Infrared thermography, ultrasound c-scan and microscope for non-destructive and destructive evaluation of 3D carbon fiber materials: a comparative study," *Proc. SPIE* **9485**, 94850X (2015).
30. N. Rajic, "Principal component thermography for flaw contrast enhancement and flaw depth characterisation in composite structures," *Compos. Struct.* **58**(4), 521–528 (2002).

**Hai Zhang** works in the Computer Vision and Systems Laboratory, Department of Electrical and Computer Engineering, Laval University in Quebec City, Canada. His current research interests include infrared thermography, x-ray computed tomography, nondestructive testing (NDT), image processing, and composite materials.

Biographies for the other authors are not available.